Volume 519, pages 339-343

LETTER

doi:10.1038/nature14240

Observational determination of surface radiative forcing by CO_2 from 2000 to 2010

D. R. Feldman[1], W. D. Collins[1,2], P. J. Gero[3], M. S. Torn[1,4], E. J. Mlawer[5] & T. R. Shippert[6]

The climatic impact of CO_2 and other greenhouse gases is usually quantified in terms of radiative forcing[1], calculated as the difference between estimates of the Earth's radiation field from pre-industrial and present-day concentrations of these gases. Radiative transfer models calculate that the increase in CO_2 since 1750 corresponds to a global annual-mean radiative forcing at the tropopause of 1.82 ± 0.19 W m^{-2} (ref. 2). However, despite widespread scientific discussion and modelling of the climate impacts of well-mixed greenhouse gases, there is little direct observational evidence of the radiative impact of increasing atmospheric CO_2. Here we present observationally based evidence of clear-sky CO_2 surface radiative forcing that is directly attributable to the increase, between 2000 and 2010, of 22 parts per million atmospheric CO_2. The time series of this forcing at the two locations—the Southern Great Plains and the North Slope of Alaska—are derived from Atmospheric Emitted Radiance Interferometer spectra[3] together with ancillary measurements and thoroughly corroborated radiative transfer calculations[4]. The time series both show statistically significant trends of 0.2 W m^{-2} per decade (with respective uncertainties of $\pm$0.06 W m^{-2} per decade and $\pm$0.07 W m^{-2} per decade) and have seasonal ranges of 0.1–0.2 W m^{-2}. This is approximately ten per cent of the trend in downwelling longwave radiation[5–7]. These results confirm theoretical predictions of the atmospheric greenhouse effect due to anthropogenic emissions, and provide empirical evidence of how rising CO_2 levels, mediated by temporal variations due to photosynthesis and respiration, are affecting the surface energy balance.

Even though Northern Hemisphere atmospheric CO_2 mixing ratios have recently exceeded 400 parts per million (ppm), few investigations have directly explored the effect of changes in well-mixed greenhouse gases on spectral and broadband radiation fluxes. In fact, doing so has proved difficult. Using data from two satellite instruments launched 26 years apart, Harries *et al.*[8] attributed systematically decreased emission in CO_2 and CH_4 spectral bands to increased opacity from, and rising concentrations in, these well-mixed greenhouse gases. However, this effort was complicated by uncertainties in instrument performance, short measurement records from each instrument, and cloud contamination[9].

In principle, CO_2 forcing can be predicted from knowledge of the atmospheric state assuming exact spectroscopy and accurate radiative transfer. Forcing can then be estimated using radiative transfer calculations with atmospheric temperature, the concentrations of radiatively active constituents including water vapour, O_3, CH_4, N_2O, and less prominent well-mixed greenhouse gases, and changes in CO_2. However, experimental validation of this forcing is needed outside the laboratory because CO_2 spectroscopy is an area of active research[10–13]. Furthermore, the fast radiative-transfer algorithms that drive regional and global climate models approximate spectroscopic absorption line-by-line calculations with errors of about 0.6 W m^{-2} (ref. 14), an amount comparable to the forcing by anthropogenic CH_4 and N_2O.

Surface forcing represents a complementary, underutilized resource with which to quantify the effects of rising CO_2 concentrations on downwelling longwave radiation. This quantity is distinct from stratosphere-adjusted radiative forcing at the tropopause, but both are fundamental measures of energy imbalance caused by well-mixed greenhouse gases[15]. The former is less than, but proportional to, the latter owing to tropospheric adjustments of sensible and latent heat[16], and is a useful metric for localized aspects of climate response[2]. We focus here on clear-sky flux changes because models predict most of the CO_2 surface forcing to occur under clear-sky conditions[15].

Specialized atmospheric observations at experimental sites in the mid-latitude continental Southern Great Plains (SGP) and the Arctic marine North Slope of Alaska (NSA) sites by the US Department of Energy Atmospheric Radiation Measurement (ARM) programme[17] produce the integrated data sets required for an independent diagnosis of the surface radiative effects of CO_2. We used spectroscopic measurements from the Atmospheric Emitted Radiance Interferometer (AERI) instrument and atmospheric state data at these two sites to test whether the impact of rising CO_2 on downwelling longwave radiation can be rigorously detected. By basing this analysis on sets of independent measurements at high temporal frequency over long duration, we empirically established how anthropogenic emissions, mediated by variations in photosynthetic activity and respiration, are altering the Earth's surface energy balance.

However, AERI spectral measurements and trends are sensitive to many different components of the atmospheric state. To interpret these measurements and attribute specific signals to rising CO_2 requires an accurate radiative-transfer model that reproduces these spectra on the basis of an independent assessment of the state of the atmosphere. The model must capture instantaneous signals and long-term trends in the spectra to determine the effects of CO_2 on diurnal to decadal timescales.

We used the Line-by-Line Radiative Transfer Model (LBLRTM)[18], which is continuously compared against other line-by-line models[4] and observations[19]. A sample clear-sky measured AERI spectrum is shown in Fig. 1a. Figure 1b shows residual spectra produced from the measurement ('obs'), minus spectra calculated ('calc') using (1) CO_2 concentrations from CarbonTracker 2011 (CT2011)[20], which is a greenhouse gas assimilation system based on measurements and modelled emission and transport; (2) methane (CH_4) profiles from CarbonTracker-CH4 (ref. 21); (3) ozone (O_3) profiles from NASA's Modern-Era Retrospective Analysis for Research and Applications (MERRA)[22]; and (4) temperature and water-vapour profiles from radiosondes (see Methods). The measured spectrum in Fig. 1a shows Planck function behaviour near the centre of the fundamental (ν_2) CO_2 band and exhibits a departure from a Planck curve in the P- and R-branches of this feature, indicating that the emission in these branches is sub-saturated and could increase with increasing CO_2. Water-vapour features, continuum emission, and O_3 emission are seen in the infrared window between 800 cm^{-1} and 1,200 cm^{-1}, and lesser features from CH_4 are seen around 1,300 cm^{-1}. Calculated transmission and the change in transmission with a 22 ppm CO_2 increase are also shown, indicating that weak vibration-rotation features in the far wings of the

[1]Lawrence Berkeley National Laboratory, Earth Sciences Division, 1 Cyclotron Road, MS 74R-316C, Berkeley, California 94720, USA. [2]University of California-Berkeley, Department of Earth and Planetary Science, 307 McCone Hall, MC 4767, Berkeley, California 94720, USA. [3]University of Wisconsin-Madison, Space Science and Engineering Center, 1225 W. Dayton Street, Madison, Wisconsin 53706, USA. [4]University of California-Berkeley, Energy and Resources Group, Berkeley, 310 Barrows Hall, MC 3050, California 94720, USA. [5]Atmospheric and Environmental Research, Inc., 131 Hartwell Avenue, Lexington, Massachusetts 02141, USA. [6]Pacific Northwest National Laboratory, Fundamental and Computational Sciences, 902 Battelle Boulevard, Richland, Washington 99354, USA.

©2015 Macmillan Publishers Limited. All rights reserved

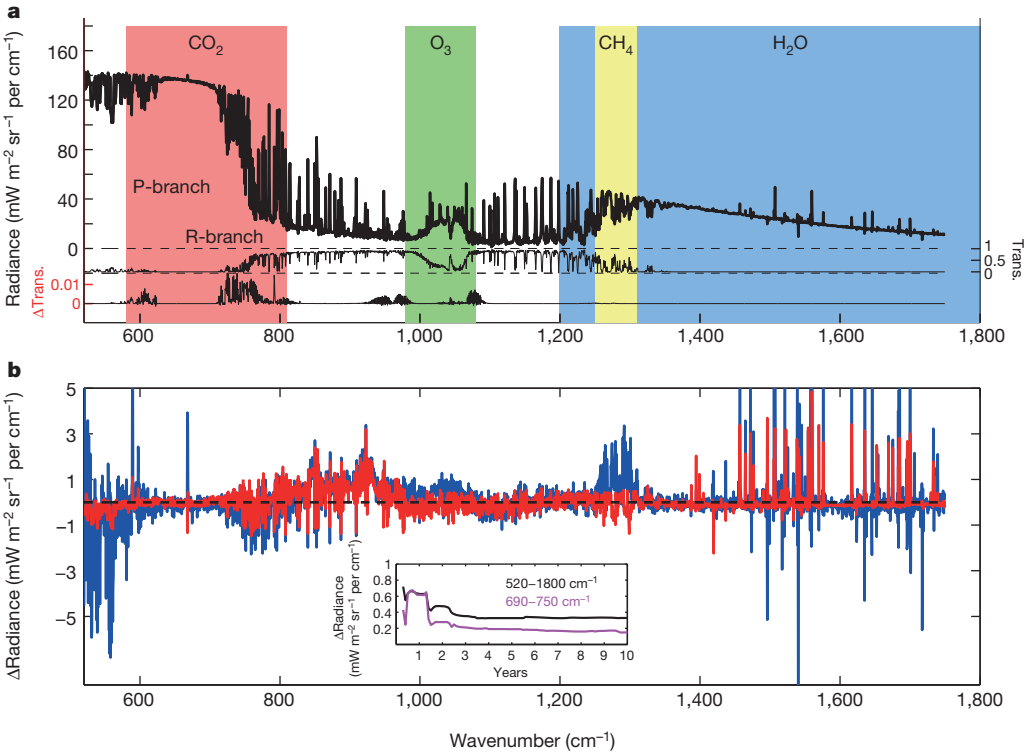

Figure 1 | AERI spectrum and residual features. **a**, Sample clear-sky AERI (channel 1) spectrum measured at SGP on 14 March 2001 2330Z, transmission calculation (Trans.) from LBLRTM, and the difference in transmission (ΔTrans.) calculated for a 22 ppm change in column-averaged CO_2 (370–392 ppm). **b**, The instantaneous spectral residual (obs − calc) (blue) and a spectral residual from observations for March 2001 (red). The inset indicates the running average of spectral residual rms of AERI Channel 01 (520–1,800 cm^{-1}) and the CO_2 R-branch (690–750 cm^{-1}).

fundamental and in the infrared window dominate surface radiative forcing from rising CO_2.

The agreement between a single measured spectrum and the LBLRTM calculation (that is, the residual) is generally within 1.5 mW m^{-2} sr^{-1} per cm^{-1}, with notable exceptions. These include the region below 550 cm^{-1} where instrumental thermal noise is present, the centre of the ν_2 CO_2 absorption feature, which is sensitive to the temperature within the instrument container, and sporadic features between 1,400 cm^{-1} and 1,800 cm^{-1} that are due to opaque water vapour lines. Nevertheless, over 90% of the residual is within a 3σ envelope established by the noise-effective radiance of 0.2 mW m^{-2} sr^{-1} per cm^{-1}. Noise in the residual spectrum does not preclude long-term spectral analysis[23] because it has no long-term bias. As highlighted in the inset of Fig. 1 the spectral root mean square (rms) of the residual decreases with the length of time over which the spectra are averaged, with asymptotes at 0.3 mW m^{-2} sr^{-1} per cm^{-1} and 0.1 mW m^{-2} sr^{-1} per cm^{-1} across the AERI band-pass and in the CO_2 R-branch, respectively.

Over the length of the observation period (2000–2010), the modelled spectra at both SGP and NSA are dominated by trends associated with the temperature and humidity structure of the atmosphere rather than the smaller signal from CO_2. The seasonal and annual trends in calculated clear-sky spectra at SGP (Fig. 2a) and NSA (Fig. 2d) are dominated by changes in the atmospheric thermodynamic state and are of opposite sign depending on the season. These signals arise from seasonally dependent clear-sky trends in temperature profiles and water vapour concentrations, as determined by radiosondes (see Methods) and must be taken into account to determine the forcing from CO_2. We therefore construct counterfactual spectra (such spectra are produced from models that keep the CO_2 concentration fixed) to simulate spectra with time-invariant CO_2, whereby we use temperature and water-vapour estimates from concurrent radiosondes to remove the thermodynamically derived radiometric signals from AERI spectra and isolate the signature of CO_2. Since most CO_2 surface forcing occurs in the absence of clouds[16], we focus on clear-sky conditions, identified using the Active Remote-Sensing of Clouds (ARSCL) Value-Added Product[24] data set.

Differences between counterfactual spectra and coincidental AERI measurements show structure in the major CO_2 absorption features as shown in Fig. 2b and e, at an order of magnitude greater than the long-term residual rms in Fig. 1b. Also shown are those spectral features for which the trend is non-zero at the 3σ level[25]. These panels show the unmistakable spectral fingerprint of CO_2. The trends in forcing are significantly ($P < 0.003$) different from zero only in the P- and R- branches of the ν_2 CO_2 band.

We can exclude alternative explanations for the change in these measurements, such as instrument calibration or the temperature, water vapour, or condensate structure of the atmosphere because they would produce significant ($P < 0.003$) trends in other spectral regions outside the CO_2 absorption bands—see Fig. 2b and e. Moreover, the spectral forcing from CO_2 is a strong function of changes in the CO_2 column concentration, and nonlinear interactions between temperature and water vapour were weak, as indicated by the lack of statistically significant differences in the seasonal and annual spectral trends in the CO_2 P- and R-branches. Therefore, the atmospheric structure of temperature and water vapour does not strongly affect CO_2 surface forcing, which is consistent with the findings of others[26,27].

Finally, when we compare counterfactual spectra with radiative transfer calculations where CO_2 is derived from CT2011, as shown in Fig. 2c and f, we again find spectral structure only in the CO_2 absorption features, thereby confirming that the model is a reliable tool for determining the surface forcing from CO_2. The utility of the counterfactual approach is further demonstrated by the probability distribution function of the difference in the rms spectral residual of AERI and LBLRTM with time-varying and fixed CO_2 concentrations for 2010 (Fig. 3). The two probability distribution functions differ substantially (two-sided t-test, $P < 0.00001$). The distribution of the mean residuals also differ significantly (two-sided t-test, $P < 0.00001$).

©2015 Macmillan Publishers Limited. All rights reserved

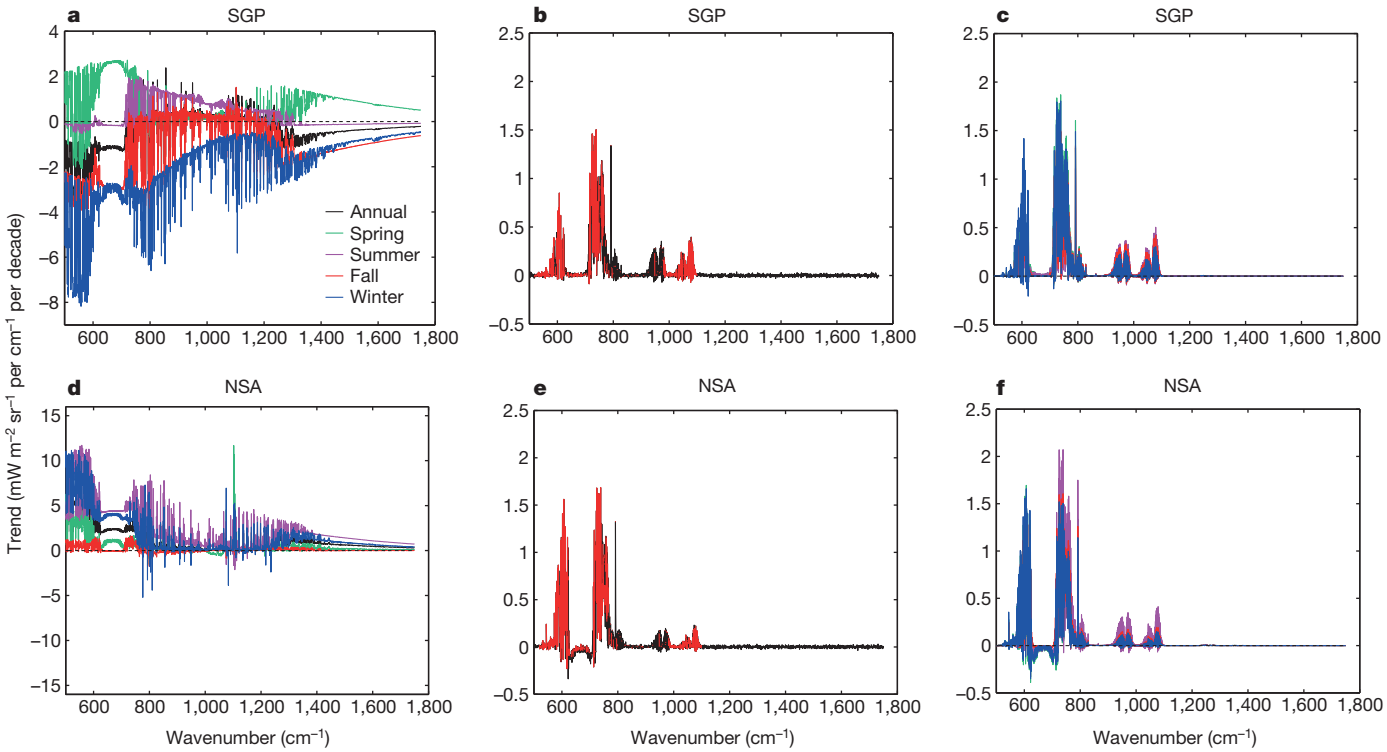

Figure 2 | Measured and modelled spectral trends for 2000–2010. **a**, Calculated (simulated) SGP AERI clear-sky seasonal and annual spectral radiance trends for 2000–2010 with temperature, water vapour, and CO_2 changes. **b**, SGP AERI annually averaged clear-sky spectral residual trends, where the residual is the difference between the measurement and a radiative-transfer calculation with CO_2 fixed at 370 ppm (in black). Red overlay indicates channel trends 3σ different from zero. **c**, As for **b** but showing residual trends from differencing calculations based on CT2011 CO_2 concentrations and CO_2 fixed at 370 ppm. **d**, As for **a** but for NSA. **e**, As for **b** but for NSA. **f**, As for **c** but for NSA.

The time series of CO_2 surface forcing, derived from differencing AERI measurements and counterfactual calculations at the SGP (Fig. 4a) and spectrally integrating and converting to flux, shows clear and increasing trends in radiative surface forcing and seasonal variability. The least-squares trend in the long-term forcing is 0.2 ± 0.06 W m^{-2} per decade and differs significantly ($P < 0.003$) from zero. The seasonal amplitude of the forcing is 0.1–0.2 W m^{-2}, closely tracking the independently assessed pattern in the average CO_2 concentration in the lowest 2 km of the atmosphere[19]. The variation in the power spectral density function of surface forcing with frequency (Fig. 4b) shows the largest peak associated with springtime photosynthesis and autumn respiration.

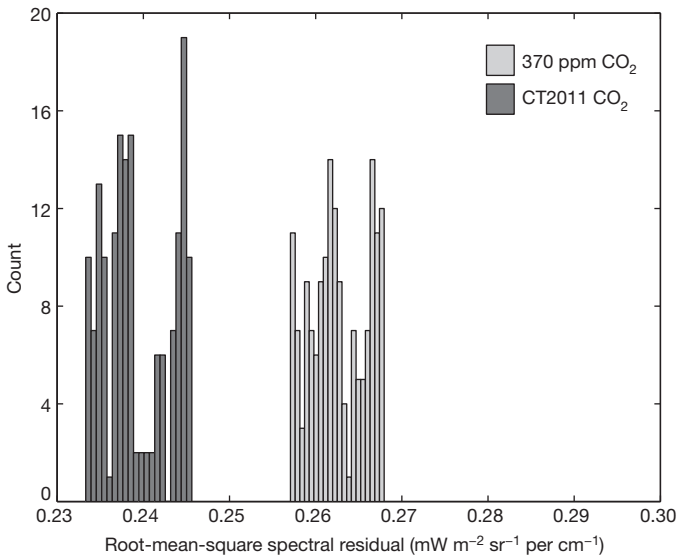

Figure 3 | Distributions of residual rms values in 2010. Histograms of rms spectral residuals (520−1,800 cm^{-1}) at SGP with time-varying CO_2 (dark grey) and a uniform 370 ppm CO_2 profile (light grey). Each count corresponds to a separate spectrum measured by AERI in 2000 or 2010.

The time-series for NSA (Fig. 4c) also has a pronounced seasonal cycle and secular trend. The range of CO_2 surface forcing is similar to that of SGP, although the higher frequency variability is much less prominent. In addition, the time series of surface forcing at NSA shows increasing variability in the latter part of the 11-year analysis record. This variability results from increased numbers of samples and fewer outages (when not all of the necessary data streams are available to derive the CO_2 forcing) at NSA from 2004 onwards. Nevertheless, the least-squares trend in CO_2 surface forcing at NSA is also 0.2 ± 0.07 W m^{-2} per decade, with a seasonal range of 0.1 W m^{-2} and differs significantly from zero ($P < 0.02$).

Increasing atmospheric CO_2 concentrations between 2000 and 2010 have led to increases in clear-sky surface radiative forcing of over 0.2 W m^{-2} at mid- and high-latitudes. Fossil fuel emissions and fires contributed substantially to the observed increase[20]. The climate perturbation from this surface forcing will be larger than the observed effect, since it has been found that the water-vapour feedback enhances greenhouse gas forcing at the surface by a factor of three[28] and will increase, largely owing to thermodynamic constraints[29]. The evolving roles of atmospheric constituents, including water vapour and CO_2 (ref. 30), in their radiative contributions to the surface energy balance can be tracked with surface spectroscopic measurements from stand-alone (or networks of) AERI instruments. If CO_2 concentrations continue to increase at the current mean annual rate of 2.1 ppm per year, these spectroscopic measurements will continue to provide robust evidence of radiative perturbations to the Earth's surface energy budget due to anthropogenic climate change, but mediated by annual variations in photosynthetic activity. These perturbations will probably influence other energy fluxes and key properties of the Earth's surface and should be explored further.

©2015 Macmillan Publishers Limited. All rights reserved

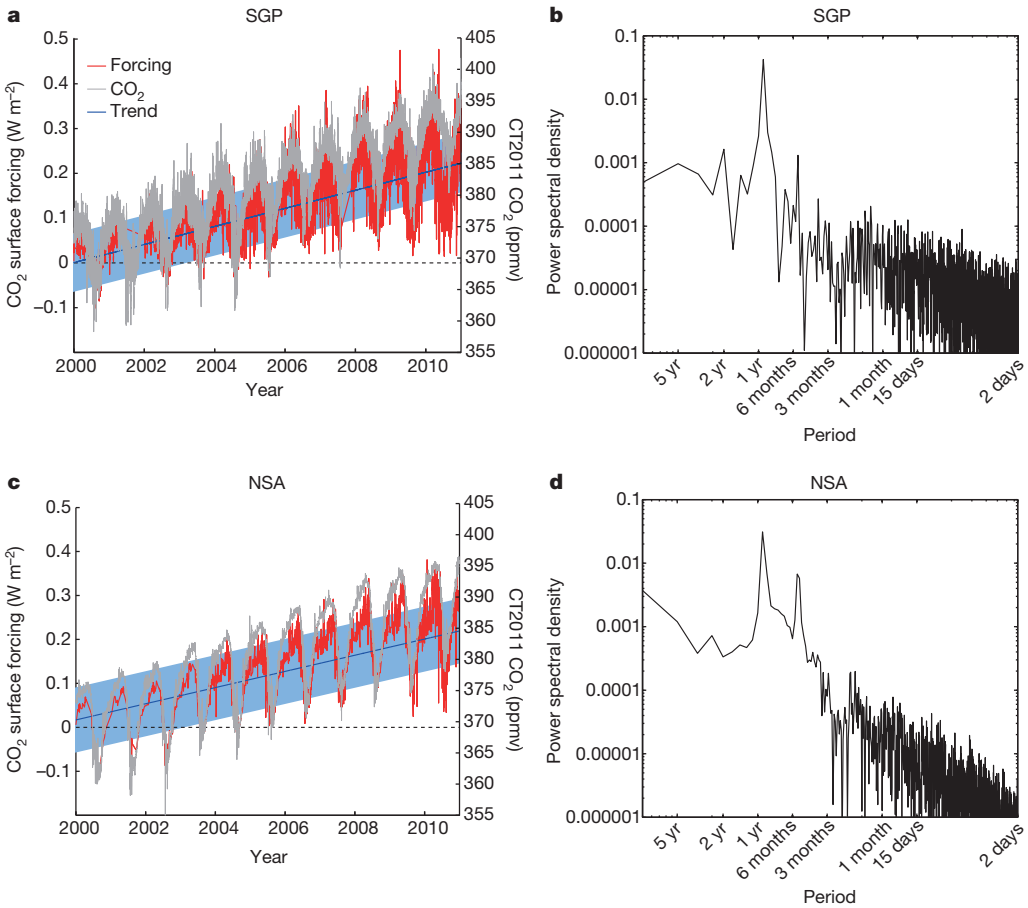

Figure 4 | Time-series of surface forcing. **a**, Time series of observed spectrally integrated (520–1,800 cm^{-1}) CO_2 surface radiative forcing at SGP (in red) with overlaid CT2011 estimate of CO_2 concentration from the surface to an altitude of 2 km (grey), and a least-squares trend of the forcing and its uncertainty (blue). **b**, Power spectral density of observed CO_2 surface radiative forcing at SGP. **c**, As for **a** but for the NSA site. **d**, As for **b** but for the NSA site.

Online Content Methods, along with any additional Extended Data display items and Source Data, are available in the online version of the paper; references unique to these sections appear only in the online paper.

Received 9 June 2014; accepted 15 January 2015.

Published online 25 February 2015.

1. Ramaswamy, V. *et al.* in *Climate Change 2001: The Scientific Basis. Contribution of Working Group I to the Third Assessment Report of the Intergovernmental Panel on Climate Change* (eds Houghton, J. T. *et al.*) 349–416 (Cambridge Univ. Press, 2001).
2. Myhre, G. *et al.* Anthropogenic and natural radiative forcing. In *Climate Change 2013: The Physical Science Basis. Contribution of Working Group I to the Fifth Assessment Report of the Intergovernmental Panel on Climate Change* (eds Stocker, T. F. *et al.*) 661 (Cambridge Univ. Press, 2013).
3. Knuteson, R. O. *et al.* Atmospheric emitted radiance interferometer. Part I: Instrument design. *J. Atmos. Ocean. Technol.* **21,** 1763–1776 (2004).
4. Oreopoulos, L. *et al.* The continual intercomparison of radiation codes: results from phase I. *J. Geophys. Res.* **117,** D06118 (2012).
5. Prata, F. The climatological record of clear-sky longwave radiation at the Earth's surface: evidence for water vapour feedback? *Int. J. Remote Sens.* **29,** 5247–5263 (2008).
6. Wild, M., Grieser, J. & Schär, C. Combined surface solar brightening and increasing greenhouse effect support recent intensification of the global land-based hydrological cycle. *Geophys. Res. Lett.* **35,** L17706 (2008).
7. Wang, K. & Liang, S. Global atmospheric downward longwave radiation over land surface under all-sky conditions from 1973 to 2008. *J. Geophys. Res.* **114,** D19101 (2009).
8. Harries, J. E., Brindley, H. E., Sagoo, P. J. & Bantges, R. J. Increases in greenhouse forcing inferred from the outgoing longwave radiation spectra of the Earth in 1970 and 1997. *Nature* **410,** 355–357 (2001).
9. Jiang, Y., Aumann, H. H., Wingyee-Lau, M. & Yung, Y. L. Climate change sensitivity evaluation from AIRS and IRIS measurements. *Proc. SPIE* **8153,** XVI, http://dx.doi.org/10.1117/12.892817 (2011).
10. Rothman, L. S. *et al.* The HITRAN2012 molecular spectroscopic database. *J. Quant. Spectrosc. Radiat.* **130,** 4–50 (2013).
11. Kochel, J.-M., Hartmann, J.-M., Camy-Peyret, C., Rodrigues, R. & Payan, S. Influence of line mixing on absorption by CO_2 Q branches in atmospheric balloon-borne spectra near 13 μm. *J. Geophys. Res.* **102** (D11), 12891–12899 (1997).
12. Niro, F., Jucks, K. & Hartmann, J.-M. Spectra calculations in central and wing regions of CO_2 IR bands. IV: Software and database for the computation of atmospheric spectra. *J. Quant. Spectrosc. Radiat.* **95,** 469–481 (2005).
13. Alvarado, M. J. *et al.* Performance of the Line-By-Line Radiative Transfer Model (LBLRTM) for temperature, water vapor, and trace gas retrievals: recent updates evaluated with IASI case studies. *Atmos. Chem. Phys.* **13,** 6687–6711 (2013).
14. Iacono, M. J. *et al.* Radiative forcing by long-lived greenhouse gases: calculations with the AER radiative transfer models. *J. Geophys. Res.* **113,** D13103 (2008).
15. Stephens, G. L. *et al.* An update on Earth's energy balance in light of the latest global observations. *Nature Geosci.* **5,** 691–696 (2012).
16. Manabe, S. & Wetherald, R. T. Thermal equilibrium of the atmosphere with a given distribution of relative humidity. *J. Atmos. Sci.* **24,** 241–259 (1967).
17. Stokes, G. M. & Schwartz, S. E. The Atmospheric Radiation Measurement (ARM) program: programmatic background and design of the cloud and radiation test bed. *Bull. Am. Meteorol. Soc.* **75,** 1201–1221 (1994).
18. Clough, S. A. *et al.* Atmospheric radiative transfer modeling: a summary of the AER codes. *J. Quant. Spectrosc. Radiat.* **91,** 233–244 (2005).
19. Turner, D. D. *et al.* Ground-based high spectral resolution observations of the entire terrestrial spectrum under extremely dry conditions. *Geophys. Res. Lett.* **39,** L10801 (2012).
20. Peters, W. *et al.* An atmospheric perspective on North American carbon dioxide exchange: CarbonTracker. *Proc. Natl Acad. Sci. USA* **104,** 18925–18930 (2007).
21. Bruhwiler, L. M. *et al.* CarbonTracker-CH4: an assimilation system for estimating emissions of atmospheric methane. *Atmos. Chem. Phys.* **14,** 8269–8293 (2014).
22. Rienecker, M. M. *et al.* MERRA: NASA's Modern-Era Retrospective Analysis for Research and Applications. *J. Clim.* **24,** 3624–3648 (2011).
23. Gero, P. J. & Turner, D. D. Long-term trends in downwelling spectral infrared radiance over the U.S. Southern Great Plains. *J. Clim.* **24,** 4831–4843 (2011).
24. Clothiaux, E. E. *et al.* Objective determination of cloud heights and radar reflectivities using a combination of active remote sensors at the ARM CART sites. *J. Appl. Meteorol.* **39,** 645–665 (2000).

©2015 Macmillan Publishers Limited. All rights reserved

25. Weatherhead, E. C. *et al.* Factors affecting the detection of trends: statistical considerations and applications to environmental data. *J. Geophys. Res.* **103** (D14), 17149–17161 (1998).
26. Haskins, R. D., Goody, R. M. & Chen, L. A statistical method for testing a general circulation model with spectrally resolved satellite data. *J. Geophys. Res.* **102,** 16563–16581 (1997).
27. Huang, Y. *et al.* Separation of longwave climate feedbacks from spectral observations. *J. Geophys. Res.* **115,** D07104 (2010).
28. Philipona, R., Dürr, B., Ohmura, A. & Ruckstuhl, C. Anthropogenic greenhouse forcing and strong water vapor feedback increase temperature in Europe. *Geophys. Res. Lett.* **32,** L19809 (2005).
29. Dessler, A. E. *et al.* Water-vapor climate feedback inferred from climate fluctuations, 2003–2008. *Geophys. Res. Lett.* **35,** L20704 (2008).
30. Haywood, J. M. *et al.* The roles of aerosol, water vapor and cloud in future global dimming/brightening. *J. Geophys. Res.* **116,** D20203 (2011).

Acknowledgements This material is based upon work supported by the US Department of Energy, Office of Science, Office of Biological and Environmental Research, Climate and Environmental Science Division, of the US Department of Energy under Award Number DE-AC02-05CH11231 as part of the Atmospheric System Research Program and the Atmospheric Radiation Measurement (ARM) Climate Research Facility Southern Great Plains. We used resources of the National Energy Research Scientific Computing Center (NERSC) under that same award. I. Williams, W. Riley, and S. Biraud of the Lawrence Berkeley National Laboratory, and D. Turner of the National Severe Storms Laboratory also provided feedback. The Broadband Heating Rate Profile (BBHRP) runs were performed using Pacific Northwest National Laboratory (PNNL) Institutional Computing at PNNL, with help from K. Cady-Pereira of Atmospheric Environmental Research, Inc., L. Riihimaki of PNNL, and D. Troyan of Brookhaven National Laboratory.

Author Contributions D.R.F. implemented the study design, performed the analysis of all measurements from the ARM sites, and wrote the manuscript. W.D.C. proposed the study design and oversaw its implementation. P.J.G. is the AERI instrument mentor and ensured the proper use of spectral measurements and quality control. M.S.T. mentored the implementation of the study and oversaw its funding. E.J.M. and T.R.S. performed calculations and analysis to determine fair-weather bias. All authors discussed the results and commented on and edited the manuscript.

Author Information Reprints and permissions information is available at www.nature.com/reprints. The authors declare no competing financial interests. Readers are welcome to comment on the online version of the paper. Correspondence and requests for materials should be addressed to D.F. (drfeldman@lbl.gov).

©2015 Macmillan Publishers Limited. All rights reserved

METHODS

The methodology for this investigation focused on analysing time series of downwelling infrared spectra to determine the effects of CO_2 on these measurements and thereby to estimate its surface radiative forcing. The analysis also used temporally coincident measurements of atmospheric temperature and water vapour, retrievals of cloud occurrence, and assimilation estimates of CO_2 to construct simulated counterfactual measurements where CO_2 is held fixed.

Code and data availability. The measurement data sets used for this analysis are freely available through the ARM data repository (http://www.arm.gov). The radiative transfer codes are also freely available at http://rtweb.aer.com. CarbonTracker results were provided by NOAA/ESRL (http://carbontracker.noaa.gov). CarbonTracker-CH4 results were provided by NOAA/ESRL (http://www.esrl.noaa.gov/gmd/ccgg/carbontracker-ch4/). The MERRA data used in this analysis are freely available for download at ftp://goldsmr3.sci.gsfc.nasa.gov/data/s4pa/MERRA/MAI3CPASM.5.2.0/. The Broadband Heating Rate Profile (BBHRP) data files, used to assess fair-weather bias, are freely available on the ARM BBHRP web page at http://www.arm.gov/data/eval/24 under http://dx.doi.org/10.5439/1163296 for the time-varying data stream and http://dx.doi.org/10.5439/1163285 for the fixed CO_2 data stream. The computer routines used in this analysis will be made available upon request.

Schematic. The schematic (Extended Data Fig. 1) shows how CO_2 surface forcing is derived from differencing Atmospheric Emitted Radiance Interferometer (AERI) observations with a model calculation based on coincidental temperature and water vapour profiles. This produces a radiance difference (called a spectral residual) that is converted to flux units through a conversion factor calculated with a radiative-transfer model based on local meteorological conditions. The spectral residual, which is driven by observations, shows features only in the CO_2 absorption bands, meaning that this is a signal just from CO_2. The integration of forcing over frequency gives a broadband forcing term and contains a secular trend due largely to anthropogenic emissions.

Data sets. Spectra observed by the AERI instrument channel 1 were analysed over the period from 2000 through the end of 2010 at the ARM SGP and NSA sites. The AERI instrument contains two channels that cover a spectral range of 520–3,020 cm^{-1} (19.2–3.3 μm) with a resolution of 0.5 cm^{-1}. Calibrated spectra are recorded every 8 min. Channel 1 observes the 520–1,800 cm^{-1} spectral region, which covers at least 99.97% of the longwave CO_2 surface forcing. The absolute calibration is traceable to NIST standards[31] and has been transferred from blackbodies with uncertainties better than 0.05 K (3σ). The resulting combined absolute uncertainty of each AERI spectrum is 1% (3σ)[32]. A summary of the AERI instrument's spectral stability can be seen in Extended Data Fig. 2, which shows the time series of effective laser wavenumber that is used to define the instrument's spectral scale. This time series exhibits a trend in the data of 4 ppm (relative) per decade around the nominal 15,799 cm^{-1} laser wavenumber. Given that the uncertainty in the AERI spectral calibration is ±5 ppm (relative) (3σ), we have confidence that there is no statistically significant drift in the AERI spectral calibration over the course of the observation period (2000–2010).

Although the AERI record extends from 1995 to the present, temporally resolved estimates of the CO_2 concentration profiles from CT2011[20], which were necessary for validation of the radiative transfer model (see below), were only available beginning in 2000 and extending through 2010, resulting in an analysis period of 11 years. Overall, the AERI is a very robust instrument that inherently produces continuous, reliable operational data. Quality control for the spectra was achieved by ensuring that valid sky spectra were being observed by the instrument with the hatch open, and that unphysical radiance values, anomalously low variances in brightness temperature across the infrared window band (800–1,200 cm^{-1}) and scenes with substantial variability in the view of the hot blackbody were removed.

CO_2 profile best estimates were obtained from CT2011, which reported eight daily profiles in the vicinity of, and which were spatially interpolated to, the SGP and NSA sites at the European Centre for Medium-Range Weather Forecasting forecast model levels on a 40° latitude by 66° longitude grid covering North America and may have spin-up effects[33]. The CT2011 assimilates data from many sources, including the average 12:00 to 16:00 local time CO_2 *in situ* measurement from the ARM Precision Carbon Dioxide Mixing Ratio System tower at 60 m altitude at SGP[34,35]. Comparisons of CT2011 against aircraft profiles collected by the ARM Carbon Measurement Experiment[36] at SGP, which are not assimilated into CT2011, exhibit a bias of less than 0.5 ppm up to 3,600 m above sea level, with a standard deviation ranging from 1 ppm in winter to 3 ppm in summer. Between 2000 and 2011, the global CO_2 concentration at the surface increased from about 369 ppm to about 392 ppm, as measured by ARM-NOAA Earth Science Research Laboratory (ESRL) flasks, while the CO_2 concentrations at SGP and NSA increased at 1.95 ppm versus 1.98 ppm per decade, respectively. Time series of CT2011 profiles at SGP and fossil fuel and fire components are shown in Extended Data Fig. 3. Output from the CT2011 data set were used to create a baseline CO_2 value of 370 ppm from which surface-forcing calculations were determined. These outputs enabled us to demonstrate that spectral residuals derived from the Line-By-Line Radiative Transfer Model (LBLRTM) version 12.2 (ref. 18) with CT2011 had a lower rms difference than spectral residuals derived from the CT2011 baseline.

Temperature and humidity profiles were gathered from the ARM Balloon-Borne Sounding System (BBSS). At the SGP site, radiosondes were launched four times per day throughout the period of analysis, while at the NSA site, radiosondes were launched two times per day over the analysis period. Three different sounding technologies have been used at both locations. At the SGP site, the Vaisala RS-80 technology was used until April 2001; the Vaisala RS-90 was used between May 2001 and February 2005; and the Vaisala RS-92 was used from February 2005 to present. At the NSA site, RS-80 technology was used through April 2002, the RS90 was used from April 2002 until January 2005, and the RS-92 technology was used since January 2005. To account for the dry bias that has been exhibited particularly by the RS-80 sensors[37], we scaled the radiosonde-reported humidity profile by the ratio of the total column water retrieved from the microwave radiometer[38,39] to the radiosonde-derived total column water. We estimate that the corrected radiosonde uncertainty is under 0.5 °C and 5% relative humidity (3σ), given the technology's stated precision and accuracy specifications. The change in radiosonde technology in the middle of the investigation could greatly complicate this analysis, and we would expect that a change in technology could introduce a jump-discontinuity in the forcing. The technology change occurred near the start of the analysis period in 2001, and the water-column amounts across the technology change differ at the $P = 0.1$ level for a two-sided t-test. However, we analysed the probability distribution function of the microwave radiometer to BBSS column water vapour both before and after the RS90 to RS92 change and did not find statistically significant differences (Extended Data Fig. 4).

Cloud clearing, which was essential to this analysis, was achieved through the ARM ARSCL Value-Added Product, which combines the Micropulse Lidar, Millimeter Wavelength Cloud Radar, and Vaisala and Belfort Ceilometers to produce six different cloud masks of varying sensitivity[24,40]. We analysed spectra collected exclusively during clear-sky conditions, as identified by the absence of clouds in all of the coincident ARSCL masks.

Thermodynamic trends. Trends in the thermodynamic state at SGP and NSA are shown in Extended Data Fig. 5. The radiosonde-derived annually averaged least-squared trend in the clear-sky temperature profile at SGP showed an increase in spring in the lowest 2 km of the atmosphere, but decreases elsewhere. Lower-atmosphere water concentrations showed trends of opposite sign depending on season and altitude. At NSA, annually averaged clear-sky temperature profile trends were positive in the lower troposphere except in spring. Lower-tropospheric humidity also increased at NSA, except in the autumn. It is important to note that these thermodynamic trends are based on clear-sky conditions only and are distinct from all-sky trends.

Still, temperature trends can have a non-zero impact on spectral downwelling longwave radiation, which can be seen in Fig. 2e, where spectral trends at wavenumbers in the near-wings of the fundamental (ν_2) CO_2 band are negative. The cause of the negative trends arises from the nonlinear interactions between CO_2 and temperature trends, especially where there is a contrast in temperature trends between the boundary layer and the free troposphere under temperature inversion conditions, which are common at the NSA site. The effects of CO_2 and temperature generally produce separable impacts on the spectral downwelling longwave radiation, especially in the weak vibration-rotation bands that dominate the observed CO_2 surface radiative forcing. However, the effects interact nonlinearly near the centre of the fundamental (ν_2) CO_2 band[27]. This nonlinearity complicates the separability of temperature and CO_2 trends over this narrow spectral range.

CarbonTracker-CH4 and MERRA data use. All radiative transfer calculations performed in this analysis used CarbonTracker-CH_4 profile information. CarbonTracker-CH_4 (ref. 21) provides eight daily profiles on a 40° latitude by 60° longitude global grid of component contributions of CH_4 to the atmospheric concentration (a background component, a component due to coal and oil/gas production, a component due to animals, rice cultivation, and waste, a component due to wetlands, soil, oceans, and insects/wild animals, a component due to emissions from fires, and a component due to emissions from oceans). We sum those components and linearly interpolate them to the ARM SGP and NSA sites in space and time to coincide with the radiosonde observation.

We also used NASA's Modern-Era Retrospective Analysis for Research and Applications (MERRA)[22] for O_3 profiles for all radiative transfer calculations. MERRA provides eight daily O_3 profiles at 42 pressure levels at 1.25° horizontal spacing and these were linearly interpolated to the ARM SGP and NSA sites in space and time to coincide with the radiosonde observation.

Radiative transfer. LBLRTM version 12.2 was used to simulate AERI spectra with and without CO_2 increases. LBLRTM was run on the 200 levels that are linearly spaced in log(pressure) onto which the radiosonde temperature and humidity

©2015 Macmillan Publishers Limited. All rights reserved

profiles have been interpolated. The conversion from spectral radiance to spectral flux was performed using spectrally dependent radiance-to-flux conversion factors determined through three-point quadrature flux calculations for each profile of atmospheric thermodynamic state corresponding to the AERI measurements following ref. 41. Histograms of the calculated distributions of the spectral conversion factor between radiance and flux are shown in Extended Data Fig. 6. These demonstrate that the conversion from radiance to flux depends on wavenumber, with stronger bands showing an Angular Distribution Model value very close to unity, indicating that the radiance is isotropic, and weaker bands having lower Angular Distribution Model values, indicating that the radiance is anisotropic.

To determine the contribution of CO_2 to surface forcing, we removed the signal associated with the other radiatively active constituents. To do this, we performed a radiative-transfer calculation using LBLRTM with observed temperature and water-vapour profiles from radiosondes (with water vapour scaled by microwave radiometer column water retrievals) and with a fixed CO_2 concentration set to 370 ppm (the CO_2 atmospheric concentration at the beginning of the analysis period) for cloud-free conditions when the AERI instrument produced calibrated spectra. We differenced these calculations against the actual AERI spectral measurements to produce a time-series of residual spectra between 2000 and the end of 2010. Since the fixed CO_2 concentration is the primary difference between the inputs to each calculation and the actual time-varying atmospheric states, the residual spectra contains the signal of changing CO_2. We integrated the spectra over frequency (wavenumber) and converted radiance to flux, based on the quadrature calculations described above, to produce a forcing value at each time step.

We used the Rapid Radiative Transfer Model[18] to perform the calculations of fair-weather bias, as described below. It calculates lower radiative forcing values than line-by-line models for the same atmospheric state[14].

Error budget. The error budget for each surface-forcing value contains contributions from several sources, including radiometric noise, instrument spectral and radiometric calibration, and residual removal. Instrument radiometric calibration is achieved through a suite of diagnostics, including detector nonlinearity characterization, electronics calibration, field-of-view testing, and routine views of the instrument blackbodies. The achieved radiometric uncertainty is better than 1% (3σ) of ambient radiance for a single observation and decreases with the number of observations. The instantaneous noise-effective spectral radiance specification for the AERI instrument is $<0.2\ \mathrm{mW\ m^{-2}\ sr^{-1}\ per\ cm^{-1}}$ for 670–1,400 $\mathrm{cm^{-1}}$, for the rms of a 2-min ambient blackbody view. Spectral calibration is achieved through routine comparisons with stable atmospheric lines and has an uncertainty of better than 0.08 $\mathrm{cm^{-1}}$ (corresponding to 5 ppm of the laser wavenumber) (3σ). Residual removal uncertainty consists of two subcomponents: (1) uncertainty in the atmospheric structure as provided by the BBSS and (2) uncertainty in the spectroscopy that informs LBLRTM. The former is derived from the radiosonde uncertainty propagated in spectral space with LBLRTM; the latter is derived from the HITRAN database uncertainty codes[10]. The effects of spectroscopic uncertainty are derived from forcing estimates with LBLRTM calculations where line parameters are modified according to stated HITRAN error codes, which report uncertainties in intensity, half-width, temperature dependence, and pressure shift for each line.

Trend determination. Both spectral trends, as shown in Fig. 2 and broadband trends, as shown in Fig. 4, are determined from a least-squares regression using Matlab's "polyfit" (http://www.mathworks.com/help/matlab/ref/polyfit.html) function of the estimate values based on clear-sky conditions only. Uncertainty in the trend was calculated from the formulae in Weatherhead *et al.*[25]. The trend in seasonal amplitude was determined from a least-squares regression from the peaks of the monthly averaged time-series of the forcing.

Fair-weather bias. One key question associated with the methods concerns the potential for fair-weather bias in this approach due to the screening of data based on the ARSCL cloud masks. A bias could occur if there is a relationship between surface forcing and cloud cover that is distinct from, and would alter the trends in, what was found under clear-sky conditions. To address this question, we have undertaken a set of calculations that follow the BBHRP[42] calculations based on the Radiatively Important Parameters Best Estimate (RIPBE)[43] Value Added Products (see http://www.arm.gov/data/eval/24 for details). This product contains broadband profiles of fluxes and heading rates throughout the atmosphere. We have recalculated BBHRP profiles at SGP for 2010 based on fixed CO_2 concentrations and compared those to the original BBHRP profiles (that contained time-varying CO_2) and subset the data that were identified as clear-sky in RIPBE (through the ARSCL flags) in order to estimate this bias. The results are shown in Extended Data Fig. 7 and indicate that the all-sky surface forcing is 0.05 $\mathrm{W\ m^{-2}}$ less than the clear-sky forcing, which represents a 25% difference in the two quantities. This finding is expected because there is non-negligible overlap between cloud absorption, which is broadband, and CO_2 absorption features, so clouds mask the forcing from CO_2. We note that the difference in clear-sky and all-sky surface radiative forcing values is not statistically significant and that the extent of the fair-weather bias depends on the occurrence frequency of cloudy conditions, which varies year-to-year at the SGP and NSA sites.

Surface versus TOA forcing. In general, several studies have found that there is a complicated relationship between surface and top-of-atmosphere (TOA) forcing, depending on the atmospheric thermodynamic and latent heating structure, with the former being less than the latter[15,44]. This is further underscored by other findings for an increase in CO_2 from 287 to 369 parts per million by volume (ppmv) which shows a forcing at the surface of 0.57 $\mathrm{W\ m^{-2}}$ and a forcing at 200 hPa of 1.92 $\mathrm{W\ m^{-2}}$ from line-by-line models[45].

To specifically address the relationship between forcing at the surface and TOA at the ARM sites, we have also undertaken a set of calculations that use the BBHRP infrastructure described above to demonstrate the relationship between surface and TOA flux changes. Results are shown in Extended Data Fig. 8, and indicate that magnitudes of the flux changes at the surface and TOA are correlated, although the TOA flux changes are larger because the downwelling surface radiation of the former quantity is distributed into sensible and latent heat. We note that the flux change at the surface and TOA is calculated by differencing fluxes with time-varying CO_2 minus fluxes with fixed CO_2 at each altitude, and the decreased emission to space and increased emission to the surface leads to flux changes of opposite sign for TOA and surface flux changes, respectively.

Vertical sensitivity. Using LBLRTM, we calculated the vertical sensitivity of broadband longwave surface forcing due to perturbations in the atmospheric state profile. These calculations were based on model atmospheres, including the US standard, the tropical, the mid-latitude summer, the mid-latitude winter, the sub-Arctic summer, and the sub-Arctic winter atmospheres, which span a broad range of atmospheric thermodynamic states[46]. We separately perturbed the temperature by 1°K, 1% water vapour, 10 ppm CO_2, 10% O_3, and 1 ppm CH_4 profiles for a 1-km-thick layer of the atmosphere from the surface to 20 km. Results are shown in Extended Data Fig. 9 and indicate that, with the exception of O_3, contributions to surface forcing are dominated by the bottom 5 km of the atmosphere, regardless of the thermodynamic state. O_3 perturbations have a more complicated vertical structure because O_3 is partially transparent in the troposphere and its concentration peaks in the stratosphere, meaning that upper-level O_3 concentration perturbations at the 10% level can have a modest impact on the surface energy balance.

31. Best, F. A. *et al.* Traceability of absolute radiometric calibration for the Atmospheric Emitted Radiance Interferometer (AERI). In *Conf. on Characterization and Radiometric Calibration for Remote Sensing (Space Dynamics Laboratory, Utah State Univ., 15–18 Sept)* http://www.calcon.sdl.usu.edu/conference/proceedings (2003).
32. Knuteson, R. O. *et al.* Atmospheric Emitted Radiance Interferometer. Part II: Instrument performance. *J. Atmos. Ocean. Technol.* **21,** 1777–1789 (2004).
33. Masarie, K. A. *et al.* Impact of CO_2 measurement bias on CarbonTracker surface flux estimates. *J. Geophys. Res.* **116,** D17305 (2011).
34. Bakwin, P. S., Tans, P. P., Zhao, C., Ussler, W. & Quesnell, E. Measurements of carbon dioxide on a very tall tower. *Tellus B.* **47,** 535–549 (1995).
35. Bakwin, P. S., Tans, P. P., Hurst, D. F. & Zhao, C. Measurements of carbon dioxide on very tall towers: results of the NOAA/CMDL program. *Tellus B.* **50,** 401–415 (1998).
36. Biraud, S. C. *et al.* A multi-year record of airborne CO_2 observations in the US Southern Great Plains. *Atmos. Meas. Technol.* **6,** 751–763 (2013).
37. Wang, J. *et al.* Corrections of humidity measurement errors from the Vaisala RS80 radiosonde—application to TOGA COARE data. *J. Atmos. Ocean. Technol.* **19,** 981–1002 (2002).
38. Liljegren, J. C. in *Microwave Radiometry and Remote Sensing of the Earth's Surface and Atmosphere* (eds Pampaloni, P. & Paloscia, S.) 433–443 (VSP Press, 1999).
39. Cimini, D., Westwater, E. R., Han, Y. & Keihm, S. J. Accuracy of ground-based microwave radiometer and balloon-borne measurements during the WVIOP2000 field experiment. *IEEE Trans. Geosci. Rem. Sens.* **41,** 2605–2615 (2003).
40. Clothiaux, E. E. *et al. The ARM Millimeter Wave Cloud Radars (MMCRs) and the Active Remote Sensing of Clouds (ARSCL) Value Added Product (VAP)* DOE Tech. Memo. ARM VAP-002.1, https://www.arm.gov/publications/tech_reports/arm-vap-002-1.pdf (US Department of Energy, 2001).
41. Li, J. Gaussian quadrature and its application to infrared radiation. *J. Atmos. Sci.* **57,** 753–765 (2000).
42. Mlawer, E. J. *et al.* The broadband heating rate profile (BBHRP) VAP. *Proc. 12th ARM Sci. Team Meet.* ARM-CONF-2002 http://www.arm.gov/publications/proceedings/conf12/extended_abs/mlawer-ej.pdf (US Department of Energy, 2002).
43. McFarlane, S., Shippert, T. & Mather, J. Radiatively Important Parameters Best Estimate (RIPBE): an ARM value-added product. DOE Tech. Rep. SC-ARM/TR-097 https://www.arm.gov/publications/tech_reports/doe-sc-arm-tr-097.pdf (US Department of Energy, 2011).
44. Andrews, T., Forster, P. M., Boucher, O., Bellouin, N. & Jones, A. Precipitation, radiative forcing and global temperature change. *Geophys. Res. Lett.* **37,** L14701 (2010).
45. Collins, W. D. *et al.* Radiative forcing by well-mixed greenhouse gases: estimates from climate models in the Intergovernmental Panel on Climate Change (IPCC) Fourth Assessment Report (AR4). *J. Geophys. Res.* **111,** D14317 (2006).
46. Anderson, G. P. *et al.* AFGL atmospheric constituent profiles (0–120 km). AFGL-TR_86-0110, http://www.dtic.mil/cgi-bin/GetTRDoc?Location=U2&doc=GetTRDoc.pdf&AD=ADA175173 (Hanscom Air Force Base, Air Force Geophysics Laboratory, 1986).

©2015 Macmillan Publishers Limited. All rights reserved

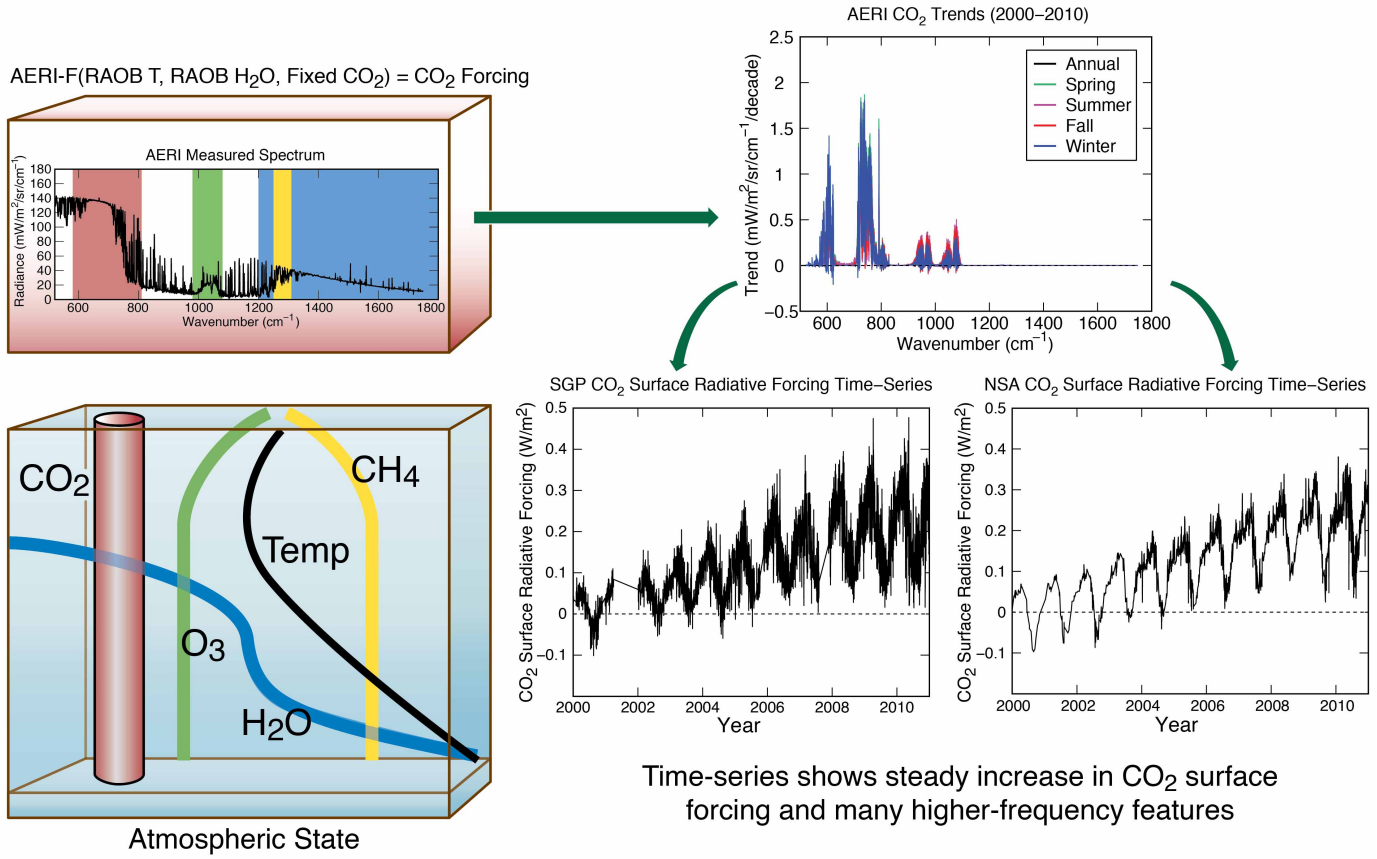

Extended Data Figure 1 | Schematic. Schematic of the derivation of surface forcing from AERI observations and calculations based on the atmospheric structure.

©2015 Macmillan Publishers Limited. All rights reserved

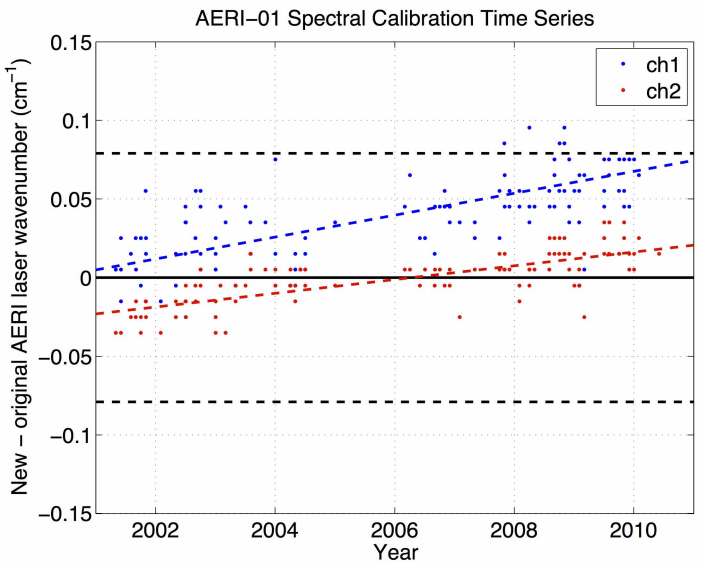

Extended Data Figure 2 | AERI instrument stability. Time series of the AERI-instrument-derived laser wavenumber around a nominal frequency of 15,799 cm^{-1}.

©2015 Macmillan Publishers Limited. All rights reserved

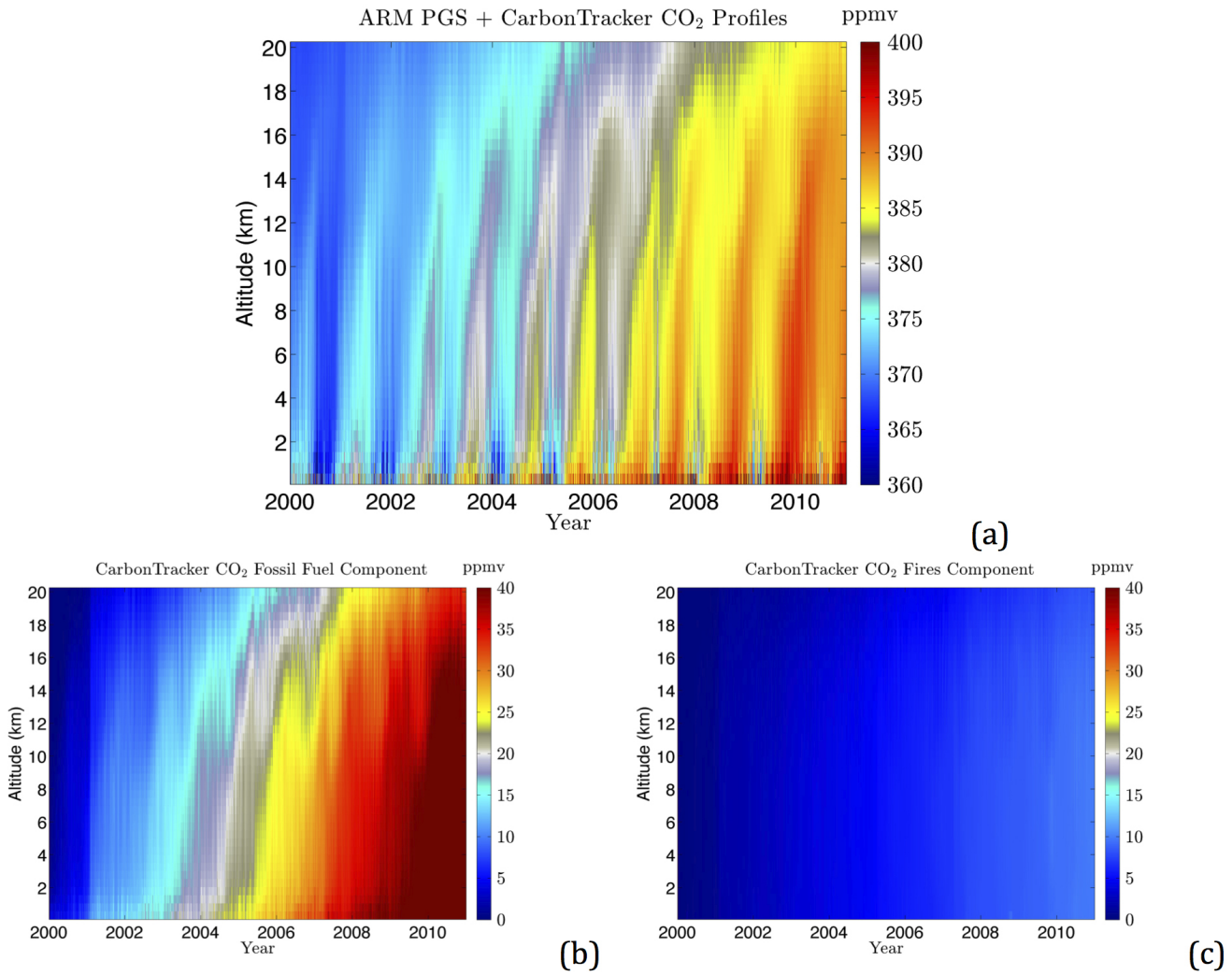

Extended Data Figure 3 | CarbonTracker profiles. **a**, CT2011 profile time series of CO_2 at the SGP site. **b**, CT2011 fossil fuel component of the CO_2 profile. **c**, CT2011 biomass burning component of the CO_2 profile. PGS, the ARM Precision Gas System Carbon Dioxide Mixing Ratio System.

©2015 Macmillan Publishers Limited. All rights reserved

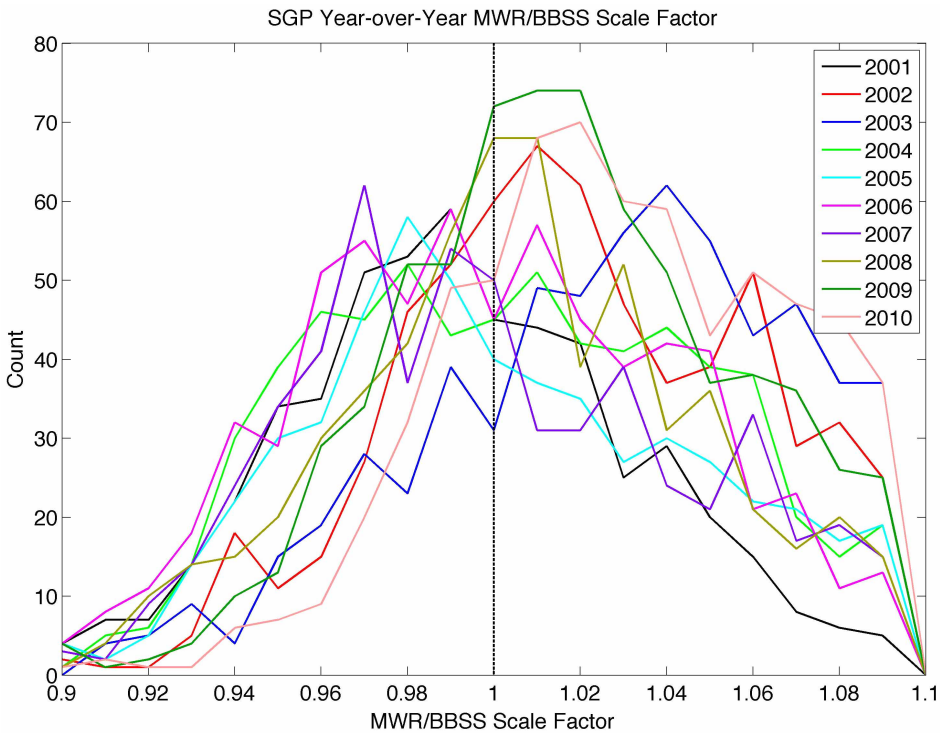

Extended Data Figure 4 | Microwave radiometer radiosonde scaling. Distribution of microwave radiometer (MWR) precipitable water vapour to the precipitable water vapour derived from radiosondes for each year of the investigation at the ARM SGP site. Each count corresponds to the scaling between a collocated radiosonde and microwave radiometer retrieval.

©2015 Macmillan Publishers Limited. All rights reserved

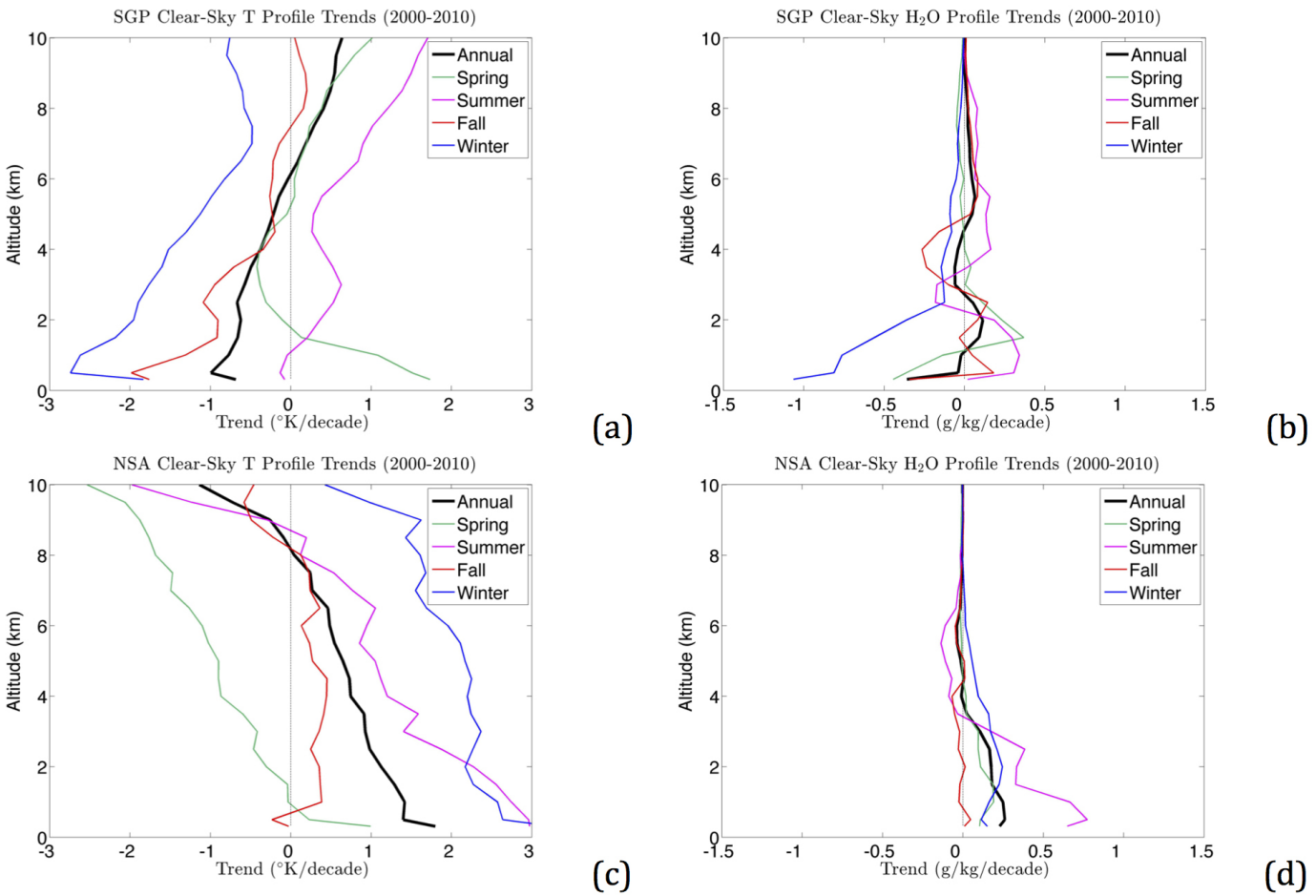

Extended Data Figure 5 | Thermodynamic trends. **a**, Annual and seasonal clear-sky temperature (T) profile trends derived from radiosondes and ARSCL data for cloud-clearing at SGP from 2000 to 2010. **b**, Same as **a** but for water vapour (H_2O) profile trends. **c**, As for **a** but temperature profile trends at NSA. **d**, As for **b** but for water vapour profile trends (in grams of water vapour per kilogram of air per decade) at NSA.

©2015 Macmillan Publishers Limited. All rights reserved

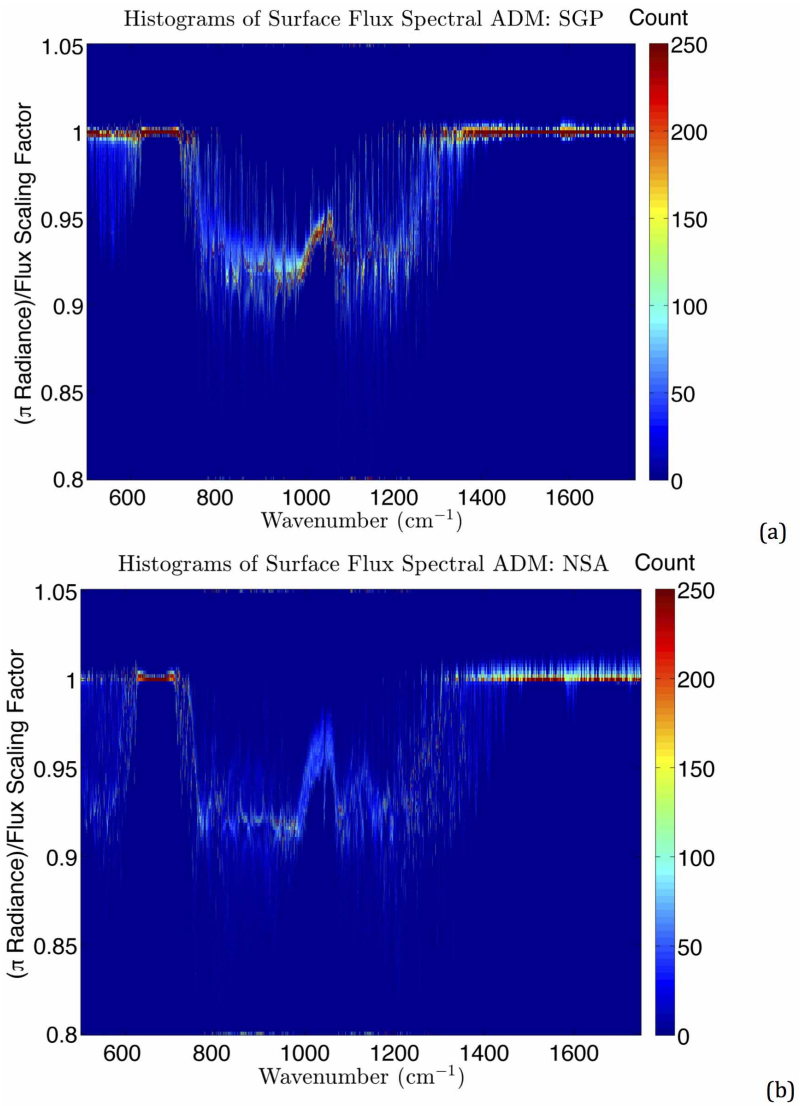

Extended Data Figure 6 | Conversion from radiance to flux. Histogram of zenith radiance to flux spectral conversion for AERI channel 1 spectral channels based on LBLRTM calculations based on the thermodynamic profiles from the ARM SGP site from 2000 to 2010. **b**, As for **a** but for the NSA site. ADM, Angular Distribution Model.

©2015 Macmillan Publishers Limited. All rights reserved

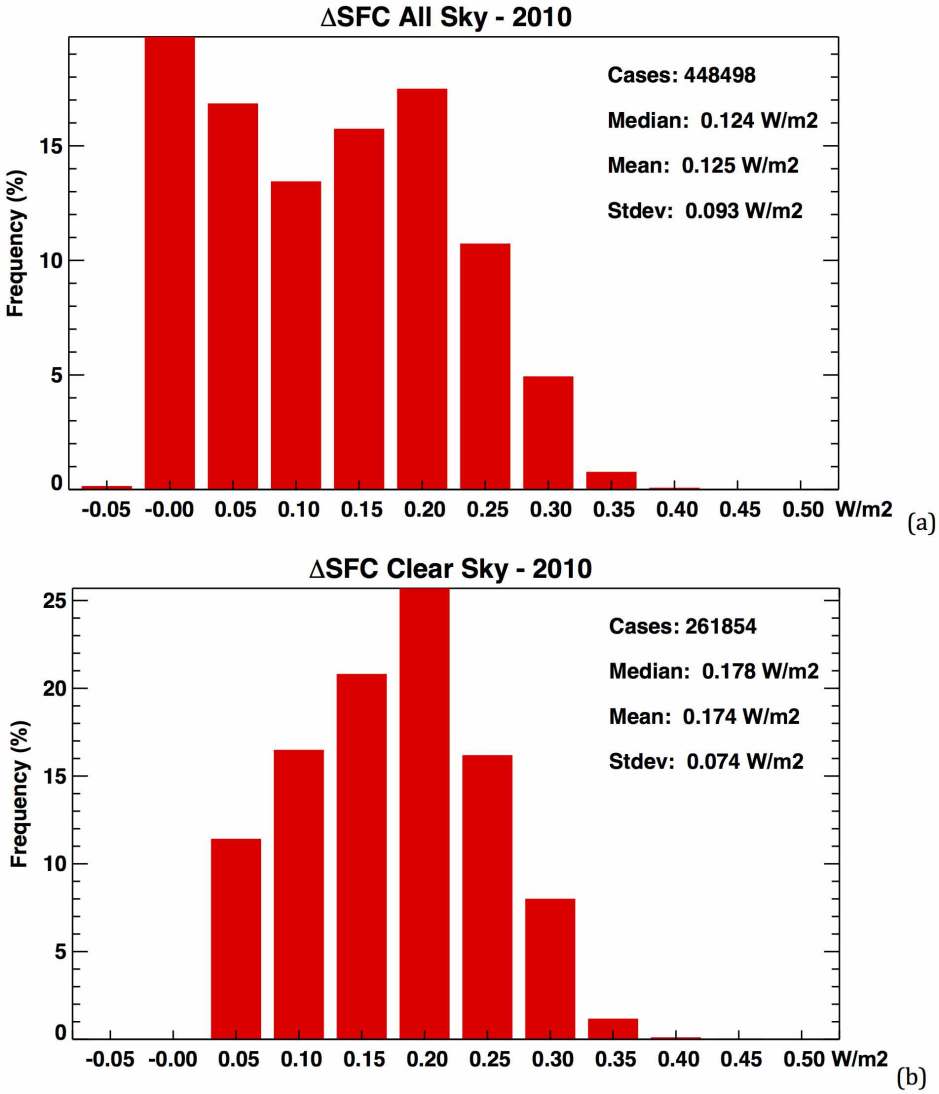

Extended Data Figure 7 | Fair-weather bias. **a**, Histogram of the difference in flux between BBHRP calculations with time-varying CO_2 and calculations where $CO_2 = 370$ ppmv for all profiles at 30-min resolution during 2010 at SGP. **b**, As for **a** but for the subset of data identified by the ARSCL as clear-sky.

©2015 Macmillan Publishers Limited. All rights reserved

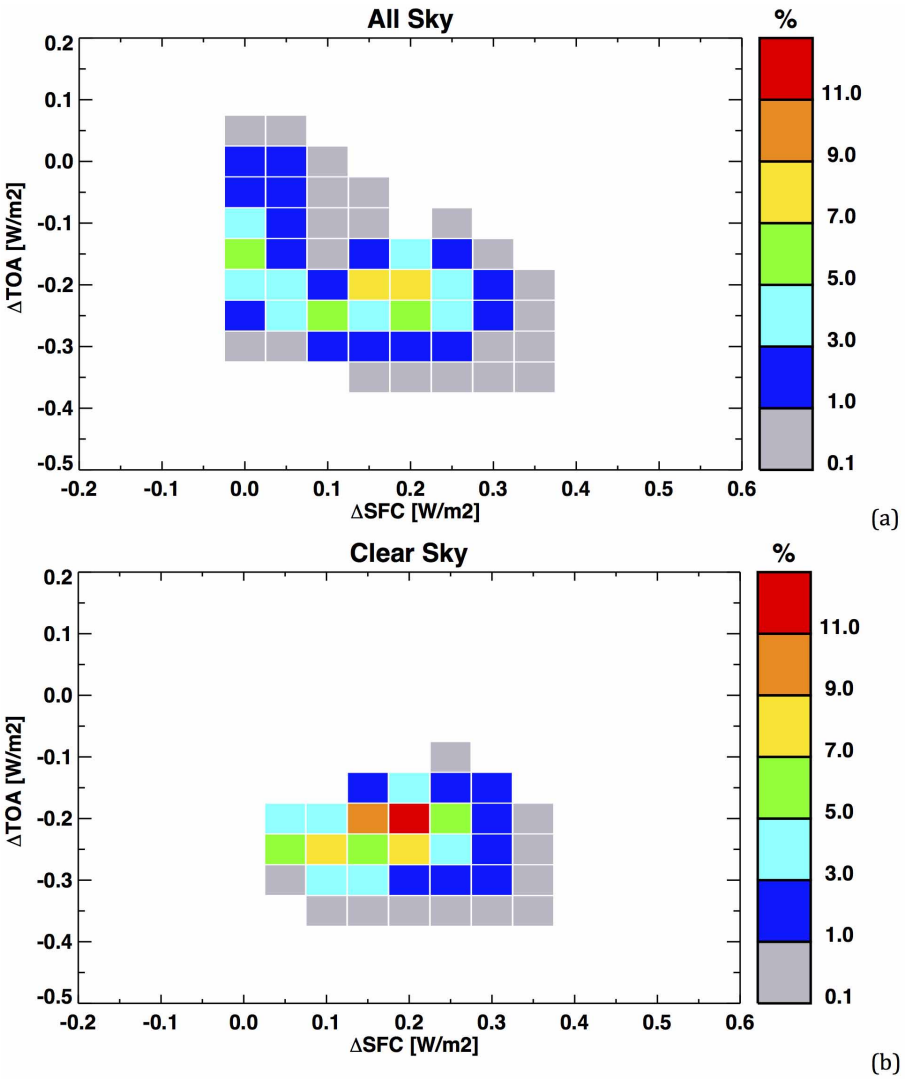

Extended Data Figure 8 | TOA and surface fluxes. **a**, Occurrence frequency (in per cent) plot of tropopause versus surface forcing based on BBHRP calculations with time-varying CO_2 and where $CO_2 = 370$ ppmv for all profiles at 30-min resolution during 2010 at SGP for all-sky conditions as identified by ARSCL flags. **b**, As for **a** but for clear-sky conditions.

©2015 Macmillan Publishers Limited. All rights reserved

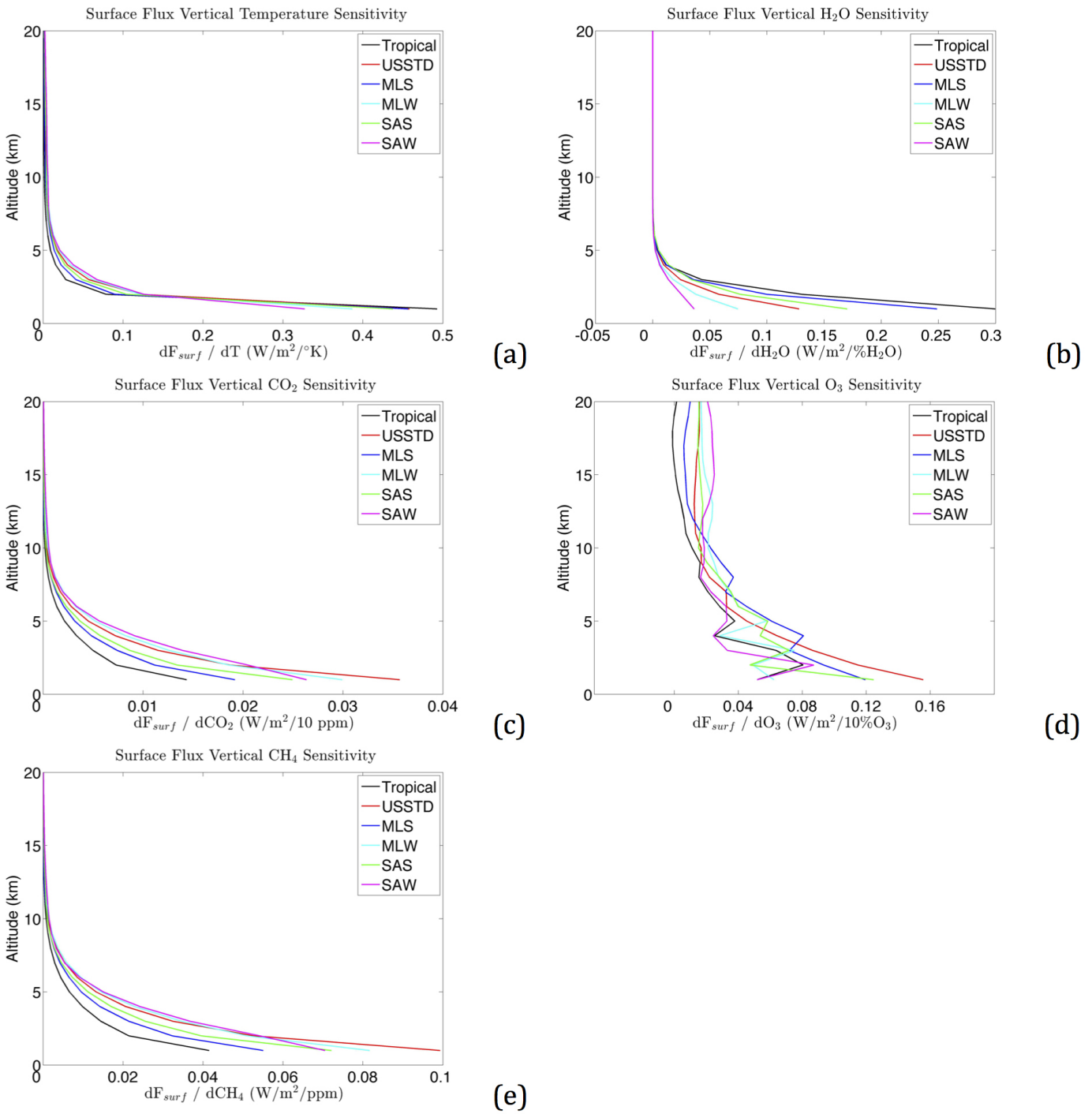

Extended Data Figure 9 | Surface flux sensitivity to atmospheric profiles. **a**, The sensitivity of the surface radiative flux (F_{surf}) to the level of a 1°K perturbation in temperature for different model atmospheres including tropical, US standard (USSTD), mid-latitude summer (MLS), mid-latitude winter (MLW), sub-Arctic summer (SAS), and sub-Arctic winter (SAW)[46]. **b**, As for **a** but level perturbations are given as percentage H_2O. **c**, As for **a** but level perturbations are 10 ppm CO_2. **d**, As for **a** but level perturbations are 10% O_3. **e**, As for **a** but level perturbations are 1 ppm CH_4.

©2015 Macmillan Publishers Limited. All rights reserved